

Article

Microwave-Assisted Synthesis of Boron-Modified TiO₂ Nanocrystals

Claudia Carlucci¹, Barbara Federica Scremin¹, Teresa Sibillano², Cinzia Giannini², Emanuela Filippo³, Patrizia Perulli³, Agostina Lina Capodilupo¹, Giuseppina Anna Corrente⁴ and Giuseppe Ciccarella^{1,3,*}

¹ Istituto Nanoscienze—CNR, National Nanotechnology Laboratory (NNL), Via Arnesano, Lecce 73100, Italy; E-Mails: claudia.carlucci@nano.cnr.it (C.C.); barbara.scremin@unisalento.it (B.F.S.); agostina.capodilupo@nano.cnr.it (A.L.C.)

² IC—CNR, Via Giovanni Amendola, 122/O, Bari 70126, Italy; E-Mails: teresa.sibillano@ic.cnr.it (T.S.); cinzia.giannini@ic.cnr.it (C.G.)

³ Department of Innovation Engineering, University of Salento, Via Monteroni, Lecce 73100, Italy; E-Mails: emanuela.filippo@unisalento.it (E.F.); patrizia.perulli@alice.it (P.P.)

⁴ University of Calabria, Via Pietro Bucci, Arcavacata di Rende, 87036, Cosenza; E-Mail: giusycorrente86@yahoo.it

* Author to whom correspondence should be addressed; E-Mail: giuseppe.ciccarella@unisalento.it; Tel.: +39-832-29 (ext. 8233).

Received: 4 April 2014; in revised form: 19 May 2014 / Accepted: 21 May 2014 /

Published: 6 June 2014

Abstract: An efficient microwave-assisted synthesis of TiO₂:(B) nanorods, using titanium tetraisopropoxide (TTIP), benzyl alcohol as the solvent, together with boric acid and oleic acid as the additive reagents, has been developed. Chemical modification of TTIP by oleic acid was demonstrated as a rational strategy to tune the shape of TiO₂ nanocrystals toward nanorod formation. The differently-shaped TiO₂:(B) nanocrystals were characterized in detail by transmission electron microscopy (TEM), inductively coupled plasma-atomic emission spectroscopy (ICP-AES), X-ray diffraction (XRD), Fourier transform infrared spectroscopy (FTIR), Raman spectroscopy and nitrogen absorption-desorption. Oleic acid coordinated on the nanocrystal surface was removed by the reduction of its carboxyl group, and the photocatalytic activity of bare TiO₂ nanocrystals, under visible light irradiation, was also evaluated. The synthesized TiO₂ anatase nanorods exhibited a good photoactivity and completely degraded Rhodamine B solution within three hours.

Keywords: microwave synthesis; TiO₂; anatase; nanocrystals; doping; photoactivity

1. Introduction

Titanium dioxide (TiO₂) is a well-studied material, used in a wide variety of applications, such as photoelectrode in dye-sensitized solar cells (DSSCs), in photochromic devices, in lithium batteries and as photocatalysts [1–5].

TiO₂ combines good electrical properties with high catalytic activity and excellent stability in many solvents over a wide pH range. A promising strategy to affect the crystallographic and optical characteristics of the final material involves the doping of TiO₂ with non-metals (N, C, S, B) [6–11].

In particular there is a growing interest in boron-doped TiO₂ materials, with low costs and easiness of processing as the key issues for planning advantageous productions [12].

Different preparation methods were explored to obtain B-modified nanoparticles that are prepared by hydrolysis of a titanium precursor in the presence of a boron-source. The typical procedures often include anaerobic conditions, different reaction steps that require many hours or days, the presence of water to hydrolyze the titanium precursor and, then, a final calcination treatment at high temperatures (400–800 °C) for some hours in order to obtain crystalline anatase [7,13] and amorphous phase composition [14] of titanium dioxide.

Non-aqueous synthetic approaches have been explored to prepare TiO₂ nanocrystals with an improved control over particle size, shape, crystallinity and surface properties [15–18].

Despite the development of many synthetic protocols at high yield, the massive production of titania nanoparticles represents still an issue. For the abovementioned reasons, it is interesting to explore new convenient synthetic routes to finely tune the properties of boron-modified titanium dioxide, TiO₂:(B), using simple one-step methods. In our previous work, a simple synthesis was applied to prepare B-modified nanocrystals using titanium tetra-isopropoxide (TTIP) together with boric acid and benzyl alcohol as the reaction solvent [18].

Usually, with the use of microwaves as the energy source to trigger chemical reactions, it is possible to obtain nanoparticles with controlled composition, crystallinity and morphology, with an improvement in the kinetics of reaction of two or three orders of magnitude [19–23].

Moreover, microwave-assisted synthesis allows one to obtain high purity titania crystalline phases at relatively low temperature, with a significant reduction of the reaction time and temperature of post-synthesis treatments. This technique offers several advantages, compared to other synthetic wet processes, as the efficient energy transfer with rapid processing of materials, leading to a clean and low-cost approach for the production of highly crystalline anatase TiO₂ nanocrystals in a high yield [24,25].

Here, we report a new, simple and rapid synthetic route to produce boron-modified anatase TiO₂ nanocrystals. The microwave-assisted synthesis took place in a single and fast step, leading to good control of the boron level and without the requirement of a post-synthetic calcination treatment of the nanocrystals. The present method constitutes a convenient compromise between the non-aqueous synthetic approach and the microwave-solvothermal method to synthesize anatase TiO₂ nanorods. We

gained also good control of particle size, shape (nanorods), crystallinity (100% anatase phase) and surface properties, with the use of TTIP as the precursor, oleic acid as the additive reagent and benzyl alcohol as the solvent, at a temperature of 210 °C with a reaction time of 45 min.

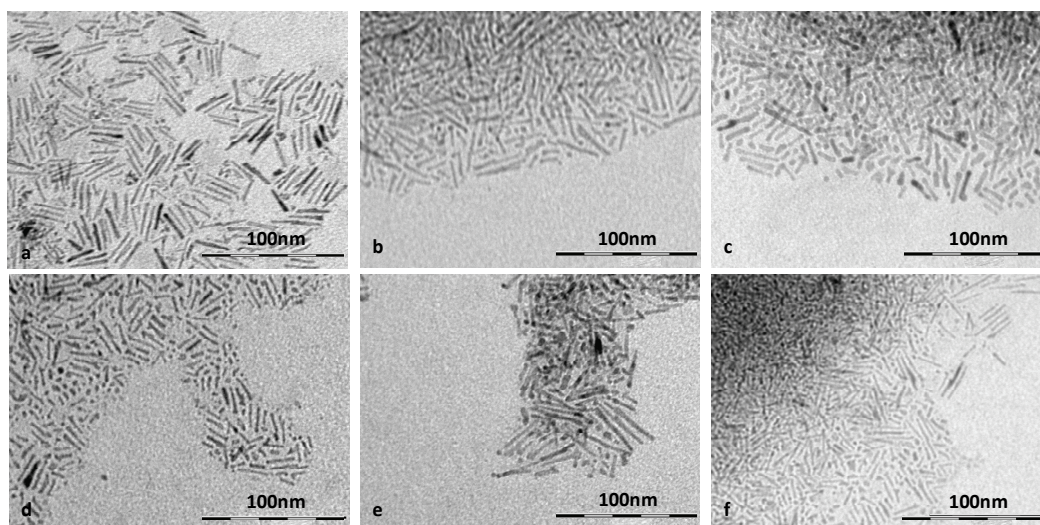
The use of benzyl alcohol was essential, as the microwave-assisted synthesis requires a polar solvent, necessary to facilitate the heating of the system. The addition of oleic acid in the reaction mixture led to a fast esterification with the simultaneous release of water, which favored the nanorod formation.

2. Results and Discussion

2.1. TEM

TEM images (Figure 1, Table 1) revealed rod-shaped nanocrystals. TEM analysis evidenced that the sample TOB1 (Figure 1a), consisted of the longest nanorods with an estimated average length of 27 nm (statistics on a hundred particles). The diameters were comparable in all the samples and were of about 3 nm. The nanoparticles size, estimated by TEM images, showed a clear dependency on the precursors nominal amounts employed in the reaction, both boric acid (BA) and oleic acid (OA), as reported in Table 1. The nanorods elongation gradually decreased as the amount of oleic acid increased for the 1:1 TTIP:BA nominal ratio, while it gradually increased as the amount of oleic acid increased for the 1:2 TTIP:BA nominal ratio. It should have been expected that increasing amounts of BA would have simply determined a decrease of the rod size, according to the limiting effect on nanocrystal growth demonstrated in a previous work, but here, the OA additions presented the ability to influence the nanocrystal growth with different trends for the two tested nominal BA ratios [18].

Figure 1. TEM images of the boron-modified nanocrystals, TiO₂(B): TOB1 (a); TOB2 (b); TOB3 (c); TOB4 (d); TOB5 (e) and TOB6 (f). Molar ratios between titanium tetra-isopropoxide (TTIP) and oleic acid are indicated in Table 1.



It can be seen that the increase in BA nominal quantity caused only a limited reduction in the nanorod size. For a deeper understanding of these trends, inductively coupled plasma-atomic emission spectroscopy (ICP-AES) analysis was performed (Table 1), which allowed us to determine the actual

ratio of B:Ti in the whole nanoparticles volume, either on the crystal surface or inside the lattice. A general increase in the B:Ti ratio was detected with the nominal 1:2 respect to the 1:1 TTIP:BA ratios. Therefore, it was observed, for the 1:1 TTIP: BA ratio, that an increase of added OA favored an increase in the amount of incorporated boron, with nanorod length reductions. For the 1:2 TTIP:BA ratio, the trend was opposite and implied a boron reduction with increasing OA content, with the consequent increase in nanorod length. Aspect ratios followed these trends, while rod diameters had almost the same value for all the samples (Table 1). This careful analysis confirms that the increased effective boron amount is a limiting factor in the nanocrystal size, as found in our previous work [18]. Moreover, OA not only tuned the morphology, driving the nanorod formation, but also influenced the effective amount of boron in the nanocrystals.

Table 1. Effective boron amount, nominal molar ratios of TTIP, boric acid (BA) and oleic acid (OA) and TEM image analysis.

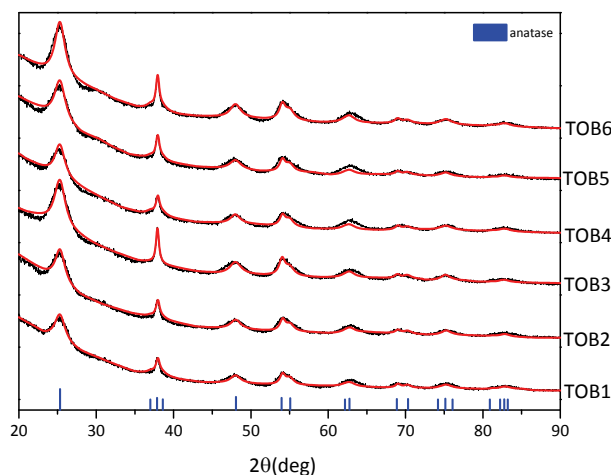
| Sample | TTIP:BA ^a | TTIP:OA ^a | B:Ti ^b | Mean Rod Length (nm) ± σ ^c | Rod Diameter (nm) ± Δ ^d | Aspect Ratio ± Δ ^e |
|--------|----------------------|----------------------|-------------------|--|---|--------------------------------------|
| TOB1 | 1:1 | 1:6 | 0.0108 | 27.0 ± 8.6 | 3.5 ± 0.6 | 7.7 ± 0.5 |
| TOB2 | 1:1 | 1:8 | 0.0240 | 18.75 ± 9.5 | 3.3 ± 0.4 | 5.7 ± 0.6 |
| TOB3 | 1:1 | 1:12 | 0.0245 | 13.6 ± 6.5 | 3.7 ± 0.5 | 3.6 ± 0.6 |
| TOB4 | 1:2 | 1:6 | 0.1138 | 14.2 ± 7.2 | 3.6 ± 0.6 | 3.9 ± 0.7 |
| TOB5 | 1:2 | 1:8 | 0.0987 | 16.5 ± 9.2 | 3.3 ± 0.4 | 5.0 ± 0.7 |
| TOB6 | 1:2 | 1:12 | 0.0641 | 22.7 ± 10.6 | 3.1 ± 0.8 | 7.3 ± 0.7 |

^a Molar ratio. The amount of TTIP was fixed (3.36 mmol); ^b B:Ti measured molar ratios, obtained by ICP-AES measurements; ^c mean value ± standard deviation, σ ; statistics on a hundred particles; ^d estimated mean value of diameter ± error of the measurement, Δ ; ^e calculated mean aspect ratio ± the calculated error, Δ .

2.2. XRD

XRD was carried out to investigate the crystalline structure of all the TiO₂:(B) nanoparticles, and the corresponding patterns are shown in Figure 2.

Figure 2. XRD patterns of TiO₂:(B) samples. Experimental data (**black curves**); Rietveld fitted profiles (**red curves**); anatase peaks positions (**blue**) markers.



The black profiles correspond to the experimental raw data, the red curves to the Rietveld fitted profiles and the blue markers to the anatase diffraction peaks positions. The XRD patterns showed also a clear inhomogeneous peak broadening, which was ascribed to crystalline domain anisotropy. This effect was analyzed with a whole-profile Rietveld-based fitting program, as described in the Experimental Section, which allowed us to determine the anatase cell parameter and crystallite apparent domain size along representative reflections, as summarized in Table 2. For anatase, the elongation direction was expected to be along the [00 l] crystallographic axis, so that the (004) and the (200) reflections mainly describe the length and the width of the nanocrystalline shape, respectively. The ratios between apparent size at (004) and at (200) reflections were also calculated and shown in Table 2. The apparent size ratios (a.s.r.) of nanocrystalline domains presented a little increase with the amount of OA, but were slightly smaller in the samples prepared with the nominal 1:2 TTIP:BA ratio. The quality of the obtained fits was checked by means of a goodness-of-fit statistical indicator (GoF). GoF values of <3–4 were found and considered to be satisfactory.

Table 2. XRD parameters of TiO₂:(B) nanocrystals and Raman shift values of two representative peaks of anatase.

| Sample | Apparent Size Ratio | Ti ^a | O ^a | 004 ^b | 200 ^b | E _g (1) ^c | E _g (3) ^c |
|--------|---------------------|-----------------|----------------|------------------|------------------|---------------------------------|---------------------------------|
| TOB1 | 2.5 | 0.97 | 2.04 | 97.67 | 35.22 | 150.6 | 652.9 |
| TOB2 | 2.7 | 0.99 | 2.59 | 101.41 | 38.63 | 151.1 | 652.6 |
| TOB3 | 4.2 | 0.95 | 2.34 | 136.56 | 35.10 | 152.1 | 654.2 |
| TOB4 | 2.5 | 1.09 | 1.88 | 102.43 | 37.19 | 150.7 | 651.2 |
| TOB5 | 3.1 | 0.89 | 2.04 | 106.75 | 34.45 | 152.0 | 656.6 |
| TOB6 | 3.1 | 1.02 | 2.23 | 114.73 | 36.61 | 151.5 | 652.0 |

^a Occupancy (theoretical values are one for Ti and two for O); ^b apparent size along the indicated directions (Å);

^c Raman shifts (cm⁻¹).

2.3. Micro Raman

Micro Raman spectra were collected on TiO₂:(B) samples and are reported in Figure 3.

From Raman features, all the samples showed the typical pattern of the anatase TiO₂ crystalline phase of six normal modes (Figure 3a) [26].

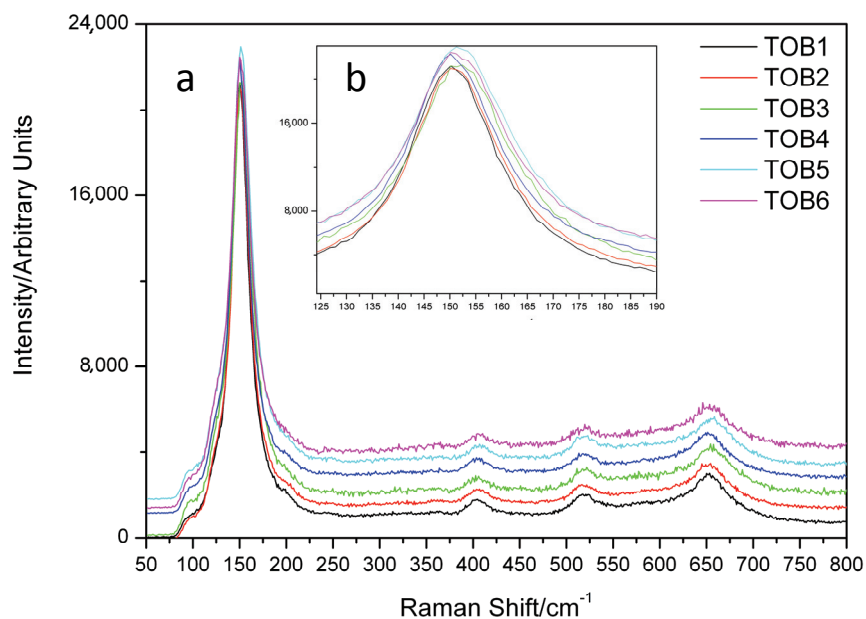
In the range of 200–800 cm⁻¹, all of the samples displayed the bands, E_g(2) (at ~197 cm⁻¹), B_{1g}(1) (at ~400 cm⁻¹), A_{1g} and B_{1g}(2) (at ~520 cm⁻¹) and E_g(3) (at ~640 cm⁻¹).

The E_g(1) band, very sensitive to the size of nanocrystalline domains and to the presence of oleate ligands [27], was detected around 150 cm⁻¹ (Figure 3b), corresponding to the 144 cm⁻¹ of bulk anatase [28]. As already mentioned, the small differences in peak wavenumbers of the E_g(1) seems poorly related to the boron content in anatase. The other five abovementioned normal modes denoted also small shifts with respect to anatase bulk values, as evidenced in nanocrystals [28].

Qualitatively, a blue shift from a 144 cm⁻¹ value of bulk anatase to about 150 cm⁻¹ is due to nanocrystal domains decreasing in size (Table 2), as commonly observed in the literature [27,28]; in detail, for the 1:1 TTIP:BA ratio, the blue shift increased as the amount of OA did; TEM aspect ratios increased; and the XRD apparent size ratio decreased (thus, the size of nanocrystalline domains decreased). In the case of 1:2 TTIP: BA samples, a maximum can be observed in correspondence of a

1:8 TTIP:OA ratio. Values of the Raman shift of two bands, sensitive to domain size and to surfactant coating [27], are reported in Table 2. The blue shifts of the $E_g(1)$ and $E_g(3)$ Raman bands resulted in being poorly sensitive to the boron amount in the anatase structure, following roughly a trend with the amount of added OA.

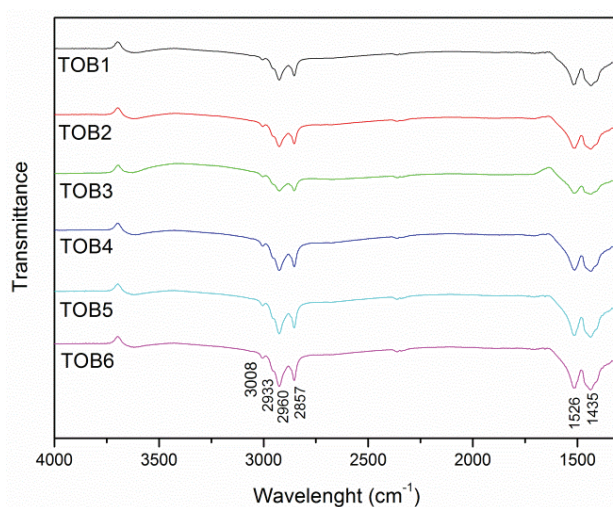
Figure 3. (a) Raman spectra of $TiO_2:(B)$ samples showing the bands corresponding to the six Raman modes of anatase TiO_2 phase; (b) $E_g(1)$ band in of the nanocrystalline samples, around 150 cm^{-1} .



2.4. FTIR

The surface presence of OA coating on boron-modified samples was evidenced in IR spectra and shown in Figure 4.

Figure 4. FTIR spectra of the $TiO_2:(B)$ samples.



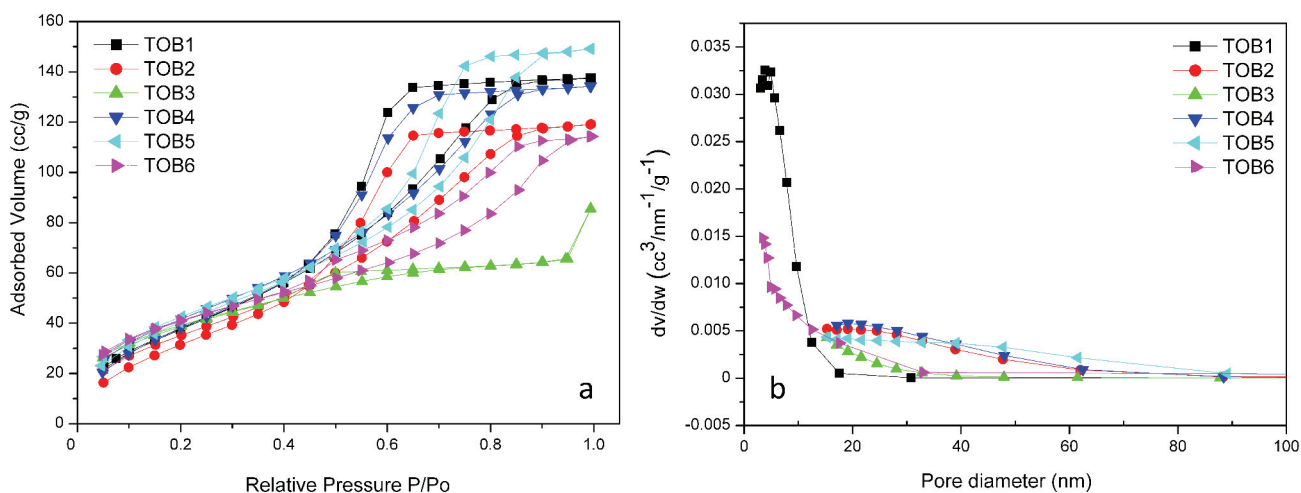
In the OA-capped TiO_2 , a weak, but definite, band at 3008 cm^{-1} was present, due to the olefinic C–H stretching. All the $\text{TiO}_2\text{:}(\text{B})$ samples exhibited the intense antisymmetric and symmetric C–H stretching vibrations (at 2933 and 2857 cm^{-1} , respectively) of the $-\text{CH}_2-$ groups in the hydrocarbon moiety. The shoulder at 2960 cm^{-1} could be associated with the asymmetric stretching of the terminal $-\text{CH}_3$ group of the alkyl chain [29].

The COO^- antisymmetric and symmetric stretching vibrations (two characteristic bands centered at 1526 and 1435 cm^{-1} , respectively) of carboxylate anions were also detected, and their frequency difference ($\sim 91\text{ cm}^{-1}$) indicated a chelating bidentate binding mode onto the TiO_2 surface [30].

2.5. BET

The surface areas were checked by Brunauer–Emmett–Teller (BET) characterization. The N_2 adsorption-desorption isotherms of the as-prepared TiO_2 nanocrystals are reported in Figure 5. The relative isotherms of the samples were of Type IV, characteristic of mesoporous materials (Figure 5a) [31].

Figure 5. (a) Nitrogen adsorption-desorption isotherms of the $\text{TiO}_2\text{:}(\text{B})$ samples; (b) pore size distribution curves, calculated according to the Barrett–Joyner–Halenda (BJH) approach.



The BET specific surface areas followed are 140.3 (TOB1), 112.9 (TOB2), 41.1 (TOB3), 112.8 (TOB4), 116.7 (TOB5) and 60.2 (TOB6) m^2/g , respectively. Thus, in the first group, where the ratio TTIP:BA is 1:1, an area decrease is observed with increasing TTIP:OA. In the second group, where TTIP:BA is 1:2, there is a similar trend for the first two samples and a decrease for the last one (with increasing TTIP:OA). Boron did not affect the area measurements as OA did.

The pore size distribution curves calculated according to the Barrett–Joyner–Halenda (BJH) approach of the as-prepared TiO_2 nanocrystals are reported in Figure 5b.

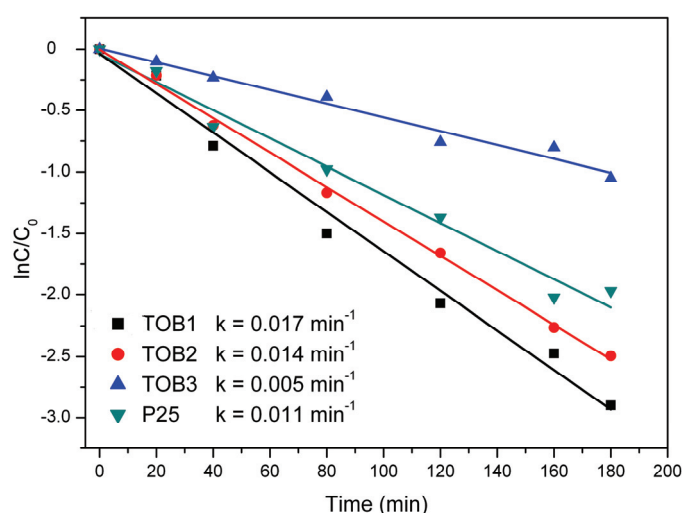
2.6. Photocatalysis

The photocatalytic performances of the $\text{TiO}_2\text{:}(\text{B})$ samples were tested by the degradation of Rhodamine B (RhB) solution under visible-light irradiation. Since BET results showed that the TOB1,

TOB2 and TOB3 samples were characterized by evident decreasing areas, we focused the photodegradation measurements on these samples. Before the photocatalytic measurements, the TiO₂ nanorods were treated under ozone flow in order to remove the surface-linked organic molecules (oleic acid), as was proven by FTIR analysis. Such a treatment allowed for obtaining a wide catalytic surface area. Blank experiments carried out on an RhB solution not containing TiO₂ proved the negligible degradation of the dye upon direct visible light. In addition, RhB/TiO₂ solutions kept in dark did not show any appreciable absorbance change over time.

The results of photocatalytic experiments are shown in Figure 6, where commercial TiO₂ Degussa P25 was used as the reference.

Figure 6. Pseudo-first-order kinetic plots for the photodegradation of RhB, where k is the apparent first-order rate constant.



The concentrations of RhB, measured from relative absorbance intensities at 550 nm at reaction times t and $t_0 = 0$, were denoted as C and C_0 , respectively.

The reaction kinetics of RhB degradation catalyzed by the different samples is reported in Figure 6, where the relationships between $\ln(C/C_0)$ and their irradiation time are shown. According to numerous literature works, the influence of the initial concentration of the solute on the photocatalytic degradation rate of the most organic compounds is described by pseudo-first-order kinetics [32].

The photocatalytic degradation plots of the experimental data fit well with pseudo-first-order reactions, and the apparent rate constants, k , were calculated from the slope of the fitting straight lines (Figure 6). Among all the samples, TOB1 presented the best activity and the highest surface area, as determined by BET. In fact, under visible light irradiation, RhB was completely degraded within three hours. Instead, TOB3 photocatalyst exhibited the lowest activity and surface area, even with respect to commercial P25.

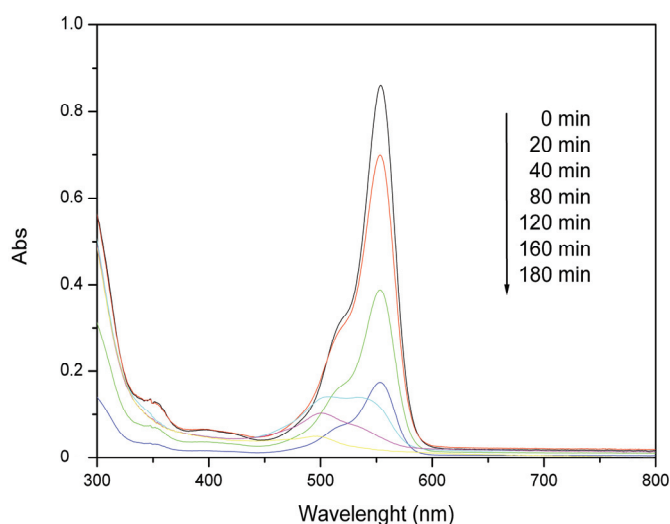
The photocatalyst TOB1 exhibited the highest rate constant ($k = 0.017 \pm 0.001 \text{ min}^{-1}$), which was approximately one and half times higher than the TiO₂ Degussa P25.

The possible photo-degradation of RhB may include four main processes: *N*-de-ethylation, chromophore cleavage, ring-opening and mineralization. RhB molecules may link on the surface of the photocatalyst through diethylamino or carboxylic groups. Under visible light irradiation and in the

presence of a photocatalyst, RhB (and subsequently, its degradation products) can absorb photons. The excited molecules thus transfer the LUMO electrons to the conductive band of TiO_2 , where the conductive electrons can react with pre-adsorbed oxygen molecules to produce reactive oxygen species, such as $\text{O}_2^{\cdot-}$, $\cdot\text{OOH}$ and $\cdot\text{OH}$. These reactive oxygen species mainly attack the auxochromic groups and induce *N*-de-ethylation of the alkyl amine group [33]. It is also postulated that photogenerated holes (h^+) can degrade suspended un-adsorbed RhB molecules and the *N*-de-ethylated products that are released in solution [34].

In Figure 7, we report the typical variation of the absorption of RhB in the presence of the photocatalyst TOB1.

Figure 7. Absorption spectrum of RhB dye degraded under visible light irradiation for 180 min using the TOB1 sample.



The peak position at 550 nm gradually decreased till its complete disappearance in less than three hours, suggesting that the fused aromatic ring structures and dye chromophores were destroyed, as highlighted by the progressive de-coloration of solutions. Thereafter, the hypsochromic (blue) shift observed was attributed to partial *N*-de-ethylation via visible light-assisted photocatalysis.

3. Experimental Section

3.1. Synthesis

All analytical-grade reagents were purchased from Sigma-Aldrich (Milan, Italy) and used without further purification. In a typical preparation, TTIP (1 mL, 3.36 mmol) was dispersed in benzyl alcohol (10 mL, 96.4 mmol), under stirring, in a Teflon[®] vessel. Boric and oleic acids were added to the reaction mixture, in different amounts, as additive reagents. Then, the reaction vessel was sealed and maintained at 210 °C for 45 min. The resulting milky suspension was centrifuged; the white precipitate was collected, washed twice with methanol and, finally, dried overnight at room temperature.

Different TTIP:OA ratios (1:6, 1:8, 1:12) and TTIP:BA molar ratios (1:1, 1:2) were used, and the samples were respectively labelled as TOB1, TOB2, TOB3, TOB4, TOB5 and TOB6 (Table 1).

3.2. Removal of Capping Layer from the TiO₂ Samples

Oleic acid coordinated on the TiO₂ nanocrystals was removed by reducing its carboxylic group. Dried TiO₂ samples were placed in a spherical glass container with cylindrical necks, and they were treated at room temperature with an ozone flow for 1 h [35]. The ozone generator, Ozonis (Septra s.r.l., Cesano Maderno, Italy), used in our experiments ensured a stable gas production of 250 mg/h.

3.3. Samples Characterization

Morphological characterizations of the TiO₂(B) nanopowders were performed using transmission electron microscopy (TEM). Images were obtained by using a Jeol Jem 1011 microscope (Jeol, Tokyo, Japan) operating at an accelerating voltage of 100 kV. The samples were prepared by dropping titania nanoparticle diluted solutions in ethanol onto 400-mesh carbon-coated copper grids and evaporating the solvent.

Inductively coupled plasma-atomic emission spectroscopy (ICP-AES) was performed with a Vista AX ICP-AES (Varian Inc., Palo Alto, CA, USA, from 2010 Agilent Technologies, Santa Clara, CA, USA) instrument. The samples were digested using a mixture of HNO₃ and HF 1:4, and ICP-AES measurements were accomplished after calibration by aqueous standards of Ti and B, with dilution ranges selected according to the expected concentrations of the elements of interest.

Powder X-ray diffraction (XRD) for the phase analysis of the nanocrystals was performed with a Rigaku (Tokyo, Japan) RINT2500 diffractometer, using Cu K α monochromatic radiation ($\lambda = 1.5418 \text{ \AA}$). The XRD patterns were recorded in the range of $2\theta = 20^\circ\text{--}90^\circ$ by coupled $\theta/2\theta$ scanning mode, using 2θ increments of 0.03° . The XRD patterns were analyzed by using a whole-profile Rietveld-based fitting program (FULLPROF) [36], according to the following procedure:

(1) The instrumental resolution function (IRF) was evaluated by fitting the XRD pattern of a LaB₆ NIST (National Institute of Standards and Technology) standard recorded under the same experimental conditions used for measuring the samples. The IRF data file was provided separately to the program in order to allow subsequent refinement of the XRD patterns of the samples.

(2) The phase composition of the samples was determined by fitting the XRD patterns with the crystal structure models of tetragonal TiO₂ nanoanatase (Inorganic Crystal Structure Database # 92363; space group: I41/amd; cell parameters: $a = b = 3.77 \text{ \AA}$ and $c = 9.43 \text{ \AA}$; $\alpha = \beta = \gamma = 90^\circ$). The weight percentage accuracy of the estimation was determined to be 5%–7% w/w;

(3) The inhomogeneous peak broadening of the anatase reflections was described by a phenomenological model based on a modified Scherrer formula:

$$\beta_{h,k,l} = \frac{\lambda}{D_{h,k,l} \cos \theta} = \frac{\lambda}{\cos \theta} \sum_{imp} a_{imp} Y_{imp}(\Theta_h, \Phi_h) \quad (1)$$

where $\beta_{h,k,l}$ was the size contribution to the integral width of the (h,k,l) reflection and Y_{imp} were the real spherical harmonics normalized according to a procedure described elsewhere [37]. After refinement of the a_{imp} coefficients, the program calculated the coherent crystal apparent domain size along each reciprocal lattice vector (h,k,l) direction. The other refinable parameters were the unit cell parameters. The background was unrefined and linearly interpolated.

Raman spectra were acquired with a inVia Raman microscope (Renishaw plc, Wotton-under-Edge, Gloucestershire, UK), edge filtered working at a 633 nm excitation wavelength; powders of the prepared samples were placed on a glass slide, and spectra were collected at room temperature. The power on the samples was around 0.8 mW, under a 50× microscope objective, giving a spot diameter of 2 μm, and a resolution of 4 cm⁻¹ was used.

Fourier transform infrared spectroscopy (FTIR) measurements in the 4000–400 cm⁻¹ spectral range were carried out using a FT/IR-6300 type A spectrophotometer (JASCO Inc, Easton, MD, USA) with the diffuse reflectance method.

The nitrogen adsorption-desorption isotherms at 77 K by BET characterization were recorded with a ASiQwin system (Quantachrome, Boynton Beach, FL, USA).

3.4. Photocatalytic Activity Measurement

The photocatalytic activities of the TiO₂ samples were evaluated by the degradation of RhB in aqueous solutions.

The photocatalyst (0.05 g) was suspended in 10 mL of water. The solution was continuously stirred for about 15 min and then added to a 50 mL RhB aqueous solution of 5 mg/L; the temperature of the RhB solution, stirred by a dynamoelectric stirrer in an open reactor, was about 25 °C.

The solution was kept in dark for 30 min before irradiation, stirred to establish an adsorption-desorption equilibrium and, then, exposed to a 150-W LOT Oriel -LS0106 tungsten halogen lamp LOT-QuantumDesign group, Darmstadt, Germany) with a 420-nm-cutoff filter, removing the UV radiation. The distance between the light source and the bottom of the solution was about 15 cm.

The concentration of RhB was monitored by colorimetry with a Cary 5000 UV-Vis spectrometer (Agilent Technologies, Santa Clara, CA, USA).

4. Conclusions

In this research work, TiO₂:(B) nanocrystals were prepared by a single and fast reaction step (a reaction time of about 45 min) by a microwave-assisted method that allows one to control the doping level, using TTIP as the precursor, BA as the boron source, OA as the capping reagent and benzyl alcohol as the solvent.

The preparation process showed that oleic acid was driving towards anatase nanorod formation, thus controlling the nanocrystal morphology. Moreover, its amount was active in controlling the effective boron quantity in the nanorods, in the investigated concentration range. The nanorod size and aspect size ratios were controlled both by the nominal added boron and by oleic acid.

The visible light photocatalytic activity was tested, and a sensible improvement with respect to commercial P25 was observed for some of the samples. Their activity was directly correlatable with the increasing BET surface areas, decreasing the XRD aspect size ratios, a smaller size of nanocrystalline domains (lower Raman shift of E_g(1) band), higher TEM aspect ratios, more than the increasing effective boron concentration in the nanorods, for the same nominal boron amount.

Acknowledgments

This research was supported by PON (National Operative Program) 254/Ric. Strengthening of a “Human and Environmental Health Research Centre” Cod. PONa3_00334, by PON n. 84/Ric. Nanomaterials for Sustainable Construction (NAMASTE) Cod. PON04a3_00107—by PO FESR (Operative Program, European Found Regional Development) 2007–2013 Nano/Micro Structure for Building materials and other productive sectors (NAMISTE) Cod. 2Y6DME5, by “Networks of Public Research Laboratories: Cod. 20, Regional Laboratory of Synthesis and Characterization of New Materials for Organic and Nanostructured Electronics, Photonics and Advanced Technologies” and by the FIRB 2009/2010 project “Integrated network for Nano Medicine (RINAME)”—RBAP114AMK_006.

Author Contributions

Claudia Carlucci performed the synthesis, FT-IR and BET; Barbara Federica Scremin performed Raman and TEM analysis; Teresa Sibillano and Cinzia Giannini performed XRD experiments; Emanuela Filippo acquired TEM images, and analyzed photocatalytic activity measurements; Patrizia Perulli and Agostina Lina Capodilupo performed capping layer removal, UV-Vis spectroscopy; Giuseppina Anna Corrente performed ICP-AES; Giuseppe Ciccarella supervised the research. The results were discussed by all the authors. Claudia Carlucci, Barbara Federica Scremin, Cinzia Giannini, Emanuela Filippo wrote the paper.

Conflicts of Interest

The authors declare no conflict of interest.

References and Notes

1. Chen, X.; Mao, S.S. Titanium Dioxide Nanomaterials: Synthesis, Properties, Modifications, and Applications. *Chem. Rev.* **2007**, *107*, 2891–2959.
2. O'Regan, B.; Gratzel, M. A low-cost, high-efficiency solar cell based on dye-sensitized colloidal TiO₂ films. *Nature* **1991**, *353*, 737–740.
3. Iuchi, K.; Ohko, Y.; Tatsuma, T.; Fujishima, A. Cathode-Separated TiO₂ Photocatalysts Applicable to a Photochromic Device Responsive to Backside Illumination. *Chem. Mater.* **2004**, *16*, 1165–1167.
4. Wagemaker, M.; van de Krol, R.; Kentgens, A.P.M.; van Well, A.A.; Mulder, F.M. Two Phase Morphology Limits Lithium Diffusion in TiO₂ (Anatase): A ⁷Li MAS NMR Study. *J. Am. Chem. Soc.* **2001**, *123*, 11454–11461.
5. Kamat, P.V. Photophysical, Photochemical and Photocatalytic Aspects of Metal Nanoparticles. *J. Phys. Chem. B* **2002**, *106*, 7729–7744.
6. Gombac, V.; de Rogatis, L.; Gasparotto, A.; Vicario, G.; Montini, T.; Barreca, D.; Balducci, G.; Fornasiero, P.; Tondello, E.; Graziani, M. TiO₂ nanopowders doped with boron and nitrogen for photocatalytic applications. *Chem. Phys.* **2007**, *339*, 111–123.

7. Ling, Q.; Sun, J.; Zhou, Q. Preparation and characterization of visible-light-driven titania photocatalyst co-doped with boron and nitrogen. *Appl. Surf. Sci.* **2008**, *254*, 3236–3241.
8. Liu, G.; Zhao, Y.; Sun, C.; Li, F.; Lu, G.Q.; Cheng, H.-M. Synergistic Effects of B/N Doping on the Visible-Light Photocatalytic Activity of Mesoporous TiO₂. *Angew. Chem. Int. Ed.* **2008**, *47*, 4516–4520.
9. Umebayashi, T.; Yamaki, T.; Itoh, H.; Asai, K. Band gap narrowing of titanium dioxide by sulfur doping. *Appl. Phys. Lett.* **2002**, *81*, 454–456.
10. Wang, H.; Lewis, J.P. Effects of dopant states on photoactivity in carbon-doped TiO₂. *J. Phys. Condens. Matter* **2005**, *17*, L209–L213.
11. Asahi, R.; Morikawa, T.; Ohwaki, T.; Aoki, K.; Taga, Y. Visible-Light Photocatalysis in Nitrogen-Doped Titanium Oxides. *Science* **2001**, *293*, 269–271.
12. Chen, D.; Yang, D.; Wang, Q.; Jiang, Z.Y. Effects of boron doping on photocatalytic activity and microstructure of titanium dioxide nanoparticles. *Ind. Eng. Chem. Res.* **2006**, *45*, 4110–4116.
13. Zhang, X.; Liu, Q. Preparation and characterization of titania photocatalyst co-doped with boron, nickel and cerium. *Mater. Lett.* **2008**, *62*, 2589–2592.
14. Zaleska, A.; Sobczak, J.W.; Grabowska, E.; Hupka, J. Preparation and photocatalytic activity of boron-modified TiO₂ under UV and visible light. *Appl. Catal. B* **2008**, *78*, 92–100.
15. De Marco, L.; Manca, M.; Giannuzzi, R.; Malara, F.; Melcarne, G.; Ciccarella, G.; Zama, I.; Cingolani, R.; Gigli, G. Novel Preparation Method of TiO₂-Nanorod-Based Photoelectrodes for Dye-Sensitized Solar Cells with Improved Light-Harvesting Efficiency. *J. Phys. Chem. C* **2010**, *114*, 4228–4236.
16. Ciccarella, G.; Martelli, C.; Matteucci, F.; Zama, I. Process for the Preparation of Titanium Dioxide having Nanometric Dimensions and Controlled Shape. Patent WO2011006659, 20 January 2011.
17. Melcarne, G.; de Marco, L.; Carlino, E.; Martina, F.; Manca, M.; Cingolani, R.; Gigli, G.; Ciccarella, G. Surfactant-free synthesis of pure anatase TiO₂ nanorods suitable for dye-sensitized solar cells. *J. Mater. Chem.* **2010**, *20*, 7248–7254.
18. Xu, H.; Picca, R.A.; de Marco, L.; Carlucci, C.; Scrascia, A.; Papadia, P.; Scremin, B.F.; Carlino, E.; Giannini, C.; Malitesta, C.; *et al.* Nonhydrolytic Route to Boron-Doped TiO₂ Nanocrystals. *Eur. J. Inorg. Chem.* **2013**, *3*, 364–374.
19. Chen, Z.; Li, W.K.; Zeng, W.J.; Li, M.S.; Xiang, J.H.; Zho, Z.H.; Huang, J.L. Microwave hydrothermal synthesis of nanocrystalline rutile. *Mater. Lett.* **2008**, *62*, 4343–4344.
20. Monti, D.; Ponrouch, A.; Estruga, M.; Palacín, M.R.; Ayllón, J.A.; Roig, A. Microwaves as a synthetic route for preparing electrochemically active TiO₂ nanoparticles. *J. Mater. Res.* **2013**, *28*, 340–347.
21. Yoon, S.; Lee, E.-S.; Manthiram, A. Microwave-Solvothermal Synthesis of Various Polymorphs of Nanostructured TiO₂ in Different Alcohol Media and Their Lithium Ion Storage Properties. *Inorg. Chem.* **2012**, *51*, 3505–3512.
22. Komarneni, S.; Roy, R.; Li, Q.H. Microwave-hydrothermal synthesis of ceramic powders. *Mater. Res. Bull.* **1992**, *27*, 1393–1405.
23. Komarneni, S.; Rajha, R.K.; Katsuki, H. Microwave-hydrothermal processing of titanium dioxide. *Mater. Chem. Phys.* **1999**, *61*, 50–54.

24. Carlucci, C.; Xu, H.; Scremin, B.F.; Giannini, C.; Altamura, D.; Carlino, E.; Videtta, V.; Conciauro, F.; Gigli, G.; Ciccarella, G. Selective synthesis of TiO₂ nanocrystals with morphology control with the microwave-solvothermal method. *CrystEngComm* **2014**, *16*, 1817–1824.
25. Xu, H.; Carlucci, C.; Scremin, B.F.; Giannini, C.; Sibillano, T.; Scrascia, A.; Capodilupo, A.L.; Gigli, G.; Ciccarella, G. Synthesis of Ultrafine Anatase Titanium Dioxide (TiO₂) Nanocrystals by the Microwave-Solvothermal Method. *J. Nanoeng. Nanomanuf.* **2014**, *4*, 28–32.
26. Ohsaka, T.; Izumi, F.; Fujiki, Y. Raman Spectrum of Anatase, TiO₂. *J. Raman Spectrosc.* **1978**, *7*, 321–324.
27. Scremin, B.F.; Belviso, M.R.; Altamura, D.; Giannini, C.; Cozzoli, P.D. Comparative Raman Study of Organic-Free and Surfactant-Capped Rod-Shaped Anatase TiO₂ Nanocrystals. *Sci. Adv. Mater.* **2014**, *6*, 923–932.
28. Georgescu, D.; Baia, L.; Ersen, O.; Baia, M.; Simon, S. Experimental assessment of the phonon confinement in TiO₂ anatase nanocrystallites by Raman spectroscopy. *J. Raman Spectrosc.* **2012**, *43*, 876–883.
29. Thistlethwaite, P.J.; Hook, M.S. Diffuse Reflectance Fourier Transform Infrared Study of the Adsorption of Oleate/Oleic Acid onto Titania. *Langmuir* **2000**, *16*, 4993–4998.
30. Nara, M.; Torii, H.; Tasumi, M. Correlation between the Vibrational Frequencies of the Carboxylate Group and the Types of Its Coordination to a Metal Ion: An *ab Initio* Molecular Orbital Study. *J. Phys. Chem.* **1996**, *100*, 19812–19817.
31. Sing, K.S.W.; Everett, D.H.; Haul, R.A.W.; Moscou, L.; Pierotti, R.A.; Roquerol, J.; Siemieniowska, T. Reporting Physisorption Data for Gas/Solid Systems with Special Reference to the Determination of Surface Area and Porosity. *Pure Appl. Chem.* **1985**, *57*, 603–619.
32. Barka, N.; Qourzal, S.; Assabbane, A.; Nounah, A.; Ichou, Y.A. Factors influencing the photocatalytic degradation of Rhodamine B by TiO₂ coated non-woven paper. *J. Photochem. Photobiol. A* **2008**, *195*, 346–351.
33. Chen, F.; Zhao, J.; Hidaka, H. Highly selective deethylation of rhodamine B: Adsorption and photooxidation pathways of the dye on the TiO₂/SiO₂ composite photocatalyst. *Int. J. Photoenergy* **2003**, *5*, 209–217.
34. Li, X.; Ye, J. Photocatalytic Degradation of Rhodamine B over Pb₃Nb₄O₁₃/Fumed SiO₂ Composite under Visible Light Irradiation. *J. Phys. Chem. C* **2007**, *111*, 13109–13116.
35. Vig, J.R. UV/ozone cleaning of surfaces. *J. Vac. Sci. Technol. A* **1985**, *3*, 1027–1034.
36. Refinement of powder (Rietveld) and single-crystal diffraction data.
37. Jarvinen, M. Application of symmetrized harmonics expansion to correction of the preferred orientation effect. *J. Appl. Crystallogr.* **1993**, *26*, 525–531.